Dynamics of the Seismicity in the Alto Tiberina Fault System revealed by a High-Resolution Template Matching Catalog

David Essing[1] and Piero Poli[2]

[1]Institut des Sciences de la Terre, Université Grenoble Alpes
[2]Université Grenoble-Alpes, Isterre Laboratory, CNRS

November 22, 2022

Abstract

The Alto Tiberina Fault system located in the Northern Apennines (Italy) consist of a low angle normal fault which radiates micro-seismicity on a constant rate and is assumed to host continuous creep. In the hanging wall, on top of the low angle normal fault, a network of syn- and antithetic high angle faults frequently hosts swarm seismic sequences, one of which has been associated to a transient aseismic deformation signal. To study in detail the dynamics related to the seismic and its relationships with aseismic deformation processes occurring in this fault system, we apply template matching on seismic data recorded at an array of borehole stations, to derive a high-resolution earthquake catalog. We then quantify the time and space clustering of the seismicity which reveals elevated clustering within the hanging wall during an aseismic deformation period. This reflects the complex evolution of aseismic slip together with the complexity of the shallow fault system. On the other hand, we observe a bimodal seismicity along the low angle normal fault, with continuous and diffuse seismicity, and rapid bursts which could suggest rapid fluid releases. Along the low angle normal fault, we additionally identify repeating earthquakes and model them assuming a creep model. Our results open the possibility for other models than the actual model of inter-seismic deformation to explain the seismicity along the Alto Tiberina low angle normal fault.

Hosted file

`essoar.10511483.1.docx` available at https://authorea.com/users/535607/articles/598808-dynamics-of-the-seismicity-in-the-alto-tiberina-fault-system-revealed-by-a-high-resolution-template-matching-catalog

Dynamics of the Seismicity in the Alto Tiberina Fault System revealed by a High-Resolution Template Matching Catalog

David Essing[1*], Piero Poli[1]

[1]ISTerre Institut des Sciences de la Terre, CNRS, Université Grenoble Alpes, France.

Corresponding author: David Essing (david.essing@univ-grenoble-alpes.fr)

Université Grenoble Alpes, ISTerre CS 40700 38058, GRENOBLE Cedex 9

Key Points:

- Template matching detects nearly half-million earthquakes along the Alto Tiberina fault system within ~3 years
- Clustered seismicity during an aseismic deformation episode reveals a complex interplay of aseismic processes and elastic interactions
- Continuous seismicity intermittent by bursts and repeating events along a LANF opens the possibility for a new model to explain the behavior

Abstract

The Alto Tiberina Fault system located in the Northern Apennines (Italy) consist of a low angle normal fault which radiates micro-seismicity on a constant rate and is assumed to host continuous creep. In the hanging wall, on top of the low angle normal fault, a network of syn- and antithetic high angle faults frequently hosts swarm seismic sequences, one of which has been associated to a transient aseismic deformation signal. To study in detail the dynamics related to the seismic and its relationships with aseismic deformation processes occurring in this fault system, we apply template matching on seismic data recorded at an array of borehole stations, to derive a high-resolution earthquake catalog. We then quantify the time and space clustering of the seismicity which reveals elevated clustering within the hanging wall during an aseismic deformation period. This reflects the complex evolution of aseismic slip together with the complexity of the shallow fault system. On the other hand, we observe a bimodal seismicity along the low angle normal fault, with continuous and diffuse seismicity, and rapid bursts which could suggest rapid fluid releases. Along the low angle normal fault, we additionally identify repeating earthquakes and model them assuming a creep model. Our results open the possibility for other models than the actual model of inter-seismic deformation to explain the seismicity along the Alto Tiberina low angle normal fault.

Plain Language Summary

In the Apennines, faults that could potentially rupture into large earthquakes can be divided into two groups by their angle between the horizon and the fault surface (dip angle) but also by their way to radiate small earthquakes. The Alto Tiberina low angle normal fault shows a small dip angle and radiates small magnitude earthquakes with a quasi-constant event-rate. In the shallow part of the

area, several faults show large dip angles and radiate thousands of small earthquakes only during certain time periods. To better understand the mechanisms responsible for the earthquakes radiated from these distinct types of faults, we apply a technique for detecting new earthquakes similar to earthquakes that are already known. This technique increases the number of detected earthquakes which helps to better analyze the behavior of the earthquakes in space and time. The results of this approach suggest that the earthquakes radiated from the high angle faults are driven by short-lived processes. The analysis of the earthquakes radiated from the low angle fault reveals continuous processes acting within this region. Additionally, this area radiates earthquakes in short time intervals from areas in close vicinity which could potentially indicate another mechanism than assumed so far.

1 Introduction

Low angle normal faults (LANF) are intriguing geological structures found in extensional tectonic regimes (Wernicke, 1995). Those structures are normal faults with a dip angle lower than $30\circ$, which should inhibit frictional fault reactivation under the well accepted Anderson-Byerlee rupture theory (Byerlee, 1978; Collettini, 2011). Nevertheless, seismically active LANFs are found in several locations around the world, such as in Greece in the Gulf of Corinth (Rietbrock et al., 1996), in Papua New Guinea in Mai'iu (Abers et al., 1997; Biemiller et al., 2020) and in Italy along the Apennines (Chiaraluce et al., 2007). Observations of seismic activity along LANFs raises the question whether these faults are capable to produce moderate-to-large magnitude earthquakes, or whether other deformation mechanisms help to accommodate the extension (e.g., Collettini, 2011; Wernicke, 1995).

A well-studied LANF is the Alto Tiberina Fault (ATF) located in the Apennines (Fig. 1a), which is thought to accommodate large portions of the overall tectonic extension of 3 mm/yr within the region (Serpelloni et al., 2005). The structure of this fault is well characterized by several seismological studies, as with deep seismic reflection profiles (Barchi et al., 2003), controlled source seismic imaging (Mirabella et al., 2004), and several seismic tomographies (e.g., Chiarabba & Amato, 2003; Pauselli et al., 2006; Piana Agostinetti et al., 2017). Further studies characterized the ATF with gravity (Boncio et al., 2000), magnetic (Collettini & Barchi, 2002), and heat flow measurements (Mirabella et al., 2004). These studies reveal a NNW trending major fault dipping $15\circ$ - $20\circ$ from the surface to at least 12-14 km depth. At depths below 4 km the fault plane is highlighted by constant micro-seismicity within a $500 - 1500$ m thick fault zone (Chiaraluce et al., 2007; Vuan et al., 2020).

The hanging wall (HW) of the LANF is dominated by several syn- and antithetic splay faults with high dipping angles of $50\circ$ - $60\circ$. The largest structure is the Gubbio fault showing a listric geometry, dipping $40\circ$ - $60\circ$ at shallow depths and bending to $10\circ$ – $15\circ$ below depths of 3 – 4 km (Mirabella et al., 2004). The HW is further characterized by high $\mathbf{v_p}/\mathbf{v_s}$ ratios, indicative of high pore-fluid pressure (Chiarabba & Amato, 2003; Piana Agostinetti et al., 2017).

The seismicity in the HW usually occurs in transient episodes with reoccurring sequences of elevated seismicity in a swarm-like behavior lacking larger events (Valoroso et al., 2017).

Focusing on the mechanical behavior of the ATF several studies (Anderlini et al., 2016; Chiaraluce et al., 2014; Collettini et al., 2011; Hreinsdóttir & Bennett, 2009; Vadacca et al., 2016) proposed that the extension in the area is accommodated to some degree by creep along the LANF. Combining a block modeling approach with GPS velocities measured at a dense GPS network in the area, Anderlini et al. (2016) inferred partial creep of 1.7 mm/yr along the LANF, with several asperities being locked. More recently the geodetic data analysis of Gualandi et al. (2017) revealed a small transient deformation signal related to a one-year long swarm-like seismic sequence starting in late 2013. This transient is thought to occur along two high-angle faults within the HW, which hosted thousands of small earthquakes with a swarm-like seismic activity (Valoroso et al., 2017). The swarm-like seismic activity was studied with a high-resolution earthquake catalog for the period between 2010 to 2014, which revealed a complex mixed mode seismicity (Valoroso et al., 2017). More recently, Vuan et al. (2020) used template matching (TM) to better characterize the seismicity occurring in the vicinity of the LANF surface and found several productive clusters indicating a time intermittent activity rate, indicative of an interaction with $M > 3$ earthquakes and slow deformation occurring within the HW.

Despite the studies cited above, several questions regarding the mechanical behavior of the ATF-system remain open. First there is the need to characterize the way in which the accommodated stress within the study area is released, if by continuous deformation along the LANF (Anderlini et al., 2016), in a transient way within the HW (Gualandi et al., 2017) or as a complex interplay of both mechanisms (Vuan et al., 2020). Another open question is related to the driving mechanism of the swarm-like seismic sequences within the HW, as a result of elastic interaction in between events or driven by transient aseismic deformation episodes (Gualandi et al., 2017). Additionally, there are still no quantitative observations assessing the role of fluids in controlling the evolution of the seismicity and the transient aseismic deformation (Chiaraluce et al., 2007; Chiodini et al., 2004; Valoroso et al., 2017), like found in other regions (Duverger et al., 2018; Ruhl et al., 2016).

To tackle the aforementioned challenges related to the deformation in the ATF system, we first derive a new high-resolution catalog of small earthquakes. This extended catalog is produced using a template matching (TM) approach (Gibbons & Ringdal, 2006) applied to an array of borehole stations (Chiaraluce et al., 2014) recording high-frequency (sampling rate of 500 Hz) and low noise data (Fig. 1b). Starting from an initial catalog of 30,000 earthquakes we detect more than 400,000 new events with magnitude as low as -2. We further analyze the detected seismicity in terms of event interaction in time and space, and systematically search and model repeating earthquakes, to infer the

role of creep along the LANF (Nadeau & McEvilly, 1999). We finally propose models to reconcile the observed seismological behavior, and reveal a complex coexistence of different processes along the ATF fault system.

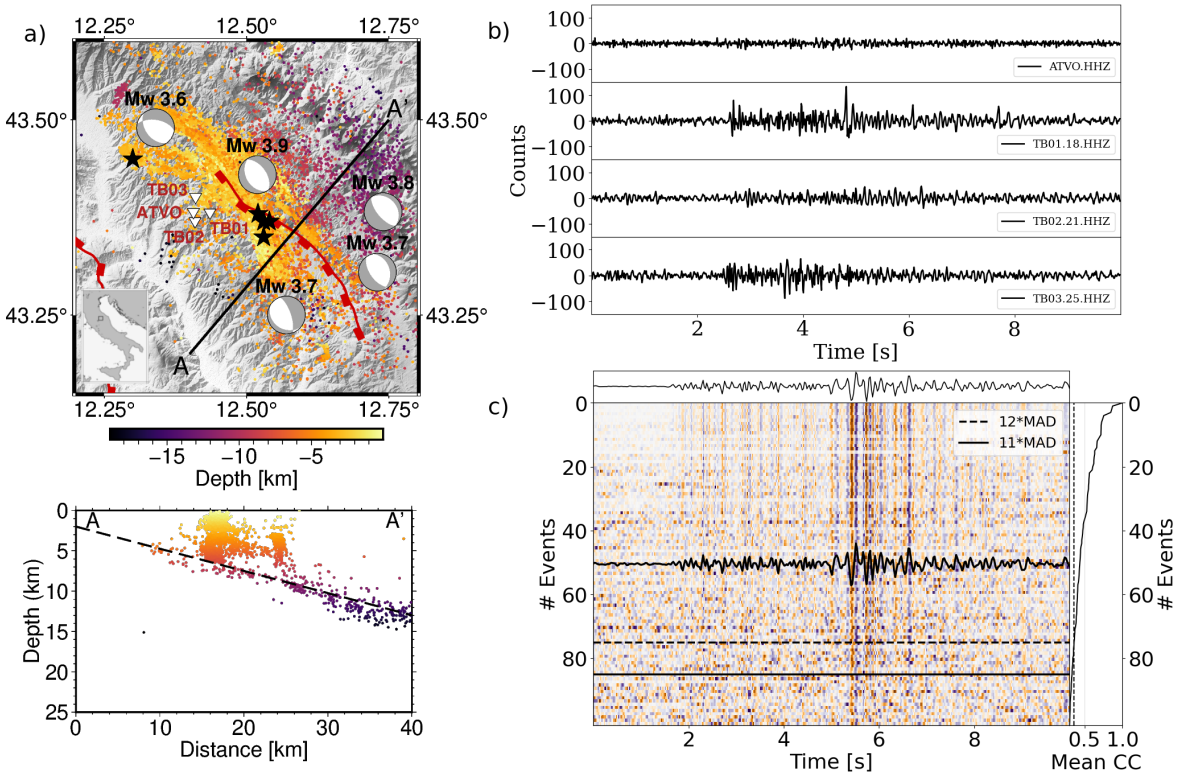

Figure 1: (a) Map and cross-section of the study area in Italy. Triangles show the locations of the borehole stations (TB0X) and one surface station (ATVO). The seismicity is plotted color-coded to indicate depth, red lines indicate fault outcrops, black stars and beach-balls indicate the locations and the focal mechanisms of the five largest events within the study period. (b) Waveforms recorded at stations indicated in (a) of a M −1.8 event (2013-04-21T20:15:15), happening northeast of the station array. (c) Waveforms recorded at TB01.BHZ of all detections made by a template event (2013-12-23T17:02:05, M = −0.98, waveform indicated on top), sorted by a decreasing CC to MAD ratio. The horizontal dashed and solid lines indicate ratios of 12 and 11, respectively. The stacked waveform considering all events of the family is indicated at Event 50 in black.

2 Detection of the Seismicity

To improve the detection of small earthquakes and ameliorate the time resolution of the seismicity in the study area, we make use of TM (Gibbons & Ringdal, 2006) and apply this array processing to data recorded at a network of borehole seismic stations (Chiaraluce et al., 2014). Figure 1a shows the network and the

seismicity used in this study. Our analysis covers a time period from July 2012 to December 2015, which encompasses the transient aseismic deformation signal (Gualandi et al., 2017) overlapping with a major earthquake swarm (Valoroso et al., 2017).

The seismic network used in this study is installed within three boreholes (Fig. 1a) two of them having one surface station and one deep station (stations TB01 and TB02), and one borehole with a surface station plus 3 stations at different depths inside the borehole (station TB03). After quality control of the data, including visual inspection in time and frequency domain, we noticed that surface stations show a general high level of noise with a daily variation. Additionally, the continuous data is contaminated by glitches and spikes. As these spurious signals are not consistent over several stations, we speculate that they originate from a source close to the sensor, probably related directly to the sensor or the digitizer. We further observe that the deepest stations are much more sensitive to small magnitude events, as illustrated in figure 1b. We thus focus our analysis on four seismometers (3-components each) located at depth (TB01 (180m), TB02 (210m), TB03 (150m) and TB03 (250m)). For all stations used, the data was sampled at 500 Hz throughout the duration of the study period.

The continuous data is analyzed using a TM approach (Gibbons & Ringdal, 2006), which is proven optimal to detect small signals with extremely low signal to noise ratios (SNR) (e.g., Beaucé et al., 2018; Beaucé et al., 2019; Sánchez-Reyes et al., 2021). With TM, the P and S waveforms of known earthquakes (templates) are correlated with continuous data recorded at different stations and different components. At every time step the average correlation coefficient (CC) over all components is used to define new detections (e.g., Beaucé et al.; 2018; Beaucé et al., 2019; Sánchez-Reyes et al., 2021).

The first step of our data processing consists of the preparation of the continuous seismic data. The daily traces are synchronized to provide seismograms of 24 hours starting at midnight. The data is then demeaned, detrended, filtered from 5 to 49 Hz, and resampled at 100 Hz. The frequency band used here differs from earlier studies in the study area (e.g., Vuan et al., 2020) which allows the detection of small magnitude events (M<0, see Cabrera et al., 2022), as they are expected to have better SNR at higher frequencies (e.g., Abercrombie, 2021). Furthermore, with the use of 5 Hz as the lower corner frequency we avoid systematically observed local noise which is strong in the frequency range from 1 to 5 Hz (Cabrera et al., 2022; Latorre et al., 2014; Poli et al., 2020; Sánchez-Reyes et al., 2021).

In a second step, we extract the potential templates from the continuous data. For this we use the earthquakes from the catalog of Valoroso et al. (2017), (Fig. 1a; Fig. 2). For the time period of interest (July 2012 until December of 2015) the catalog contains 34,923 events, which are precisely relocated using a double difference approach (Valoroso et al., 2017). In our work, we define a template as 1.2 s long P and S waveforms starting 0.4 s before the theoretical arrival time at each seismometer. The theoretical arrival times are calculated with a

local 1D velocity model (Chiaraluce et al., 2007; Tab. S1). P waveforms are extracted from the vertical seismometer component, while the S waveforms from the horizontal components. For each potential template we calculate the root-mean-square (rms) amplitude within a noise window (1.2 s long time window previous to the P wave arrival) and relate this to the rms amplitude within the P and S waves windows to obtain the SNR for each template. Only templates with a SNR > 3 at more than 8 seismometer components are retained for further analysis. This step reduces the number of templates for the final run to 28,903.

We then use each template to scan the daily continuous data with a sliding window of one sample. This computation implies the calculation of 10^{14} correlations per component. To perform this large analysis, we use the Fast Matched-Filter (FMF) code of Beaucé et al. (2018) based on a parallel GPU framework. The processing was performed using a single NVIDIA Tesla V100 GPU with NVLink, and implied 2800 h of computation. For each template we obtain daily traces of the CC averaged over all seismometer components, which are then used to extract detections of new events. To that scope, we estimate the median absolute deviation (MAD) for the daily trace of the CCs and define a new detected event when the CC at a sample exceeds the daily MAD by a factor of 10.

This preliminary threshold was chosen from tests made with a subset of data and using low SNR templates and is further in good agreement with other studies (Cabrera et al., 2022; Sánchez-Reyes et al., 2021; Shelly, 2020). With these parameters we obtain a first set of detections, which includes redundant ones (e.g., new detections identified by multiple templates). This redundancy results in event detections with an interevent time smaller than the template window length (1.2 s). Therefore, we decluster this first set of detections using the inter-event arrival time at the seismometer network. In this study we retain events with an average inter-event arrival time at the network larger than 1.2 s, which corresponds to the window length of the template. This approach allows to detect events with inter-event times even below 1.2 s if the hypocentral distances in between them is large enough. However, within a group of redundant detections, the CC ranges from ~0.2 to values of up to 1 if an auto-detection is included. In each group of redundant detections, we retain only the ones with the highest CC for the final extended catalog. After the declustering the extended catalog consists of 630,265 detected events, that is 21 times the number of events within the initial catalog.

Each newly detected event is assigned to the location of the template which detected it (Valoroso et al., 2017). We estimate the magnitude of a newly detected event by measuring the ratio of the waveform amplitudes between the template and the newly detected event (Cabrera et al., 2022; Peng & Zhao, 2009). The ratio is taken from the absolute mean value within a window length of 1.2 s during the P-arrival on every component. Then, the new magnitude is estimated by adding the logarithm to the base of 10 of the median ratio of all components to the template's magnitude. This approach assumes a change of

10 in the amplitude as a change of 1 unit in magnitude (Cabrera et al., 2022; Peng & Zhao, 2009).

We subsequently perform quality control on the extended catalog, to ensure that only real detections of good quality are included. This step involves visual inspection of events detected by single templates (Fig. 1c). We thus plotted 10s of the waveforms for all detections made by one template sorted by a decreasing CC to MAD ratio (Fig. 1c). New detected events above the dashed line have a ratio >12, while detections above the solid line have a ratio > 11. From the figure 1c, we can see clear P wave arrivals for the first 30 detections, while P waves fade out around detection number 40. The S wave arrivals are generally more prominent and can be seen for almost all detections, fading out below ratios of 11.

We performed the aforementioned procedure of visual inspection on randomly chosen families. The approach led us to retain only detections with a CC to MAD ratio > 12 as new events. This choice leads to a final catalog of 447,834 events which is an extension of the initial catalog (34,923 events) by a factor of 12, in agreement with studies from other areas using a similar approach (e.g., Gibbons & Ringdal, 2006; Sánchez-Reyes et al., 2021; Shelly, 2020).

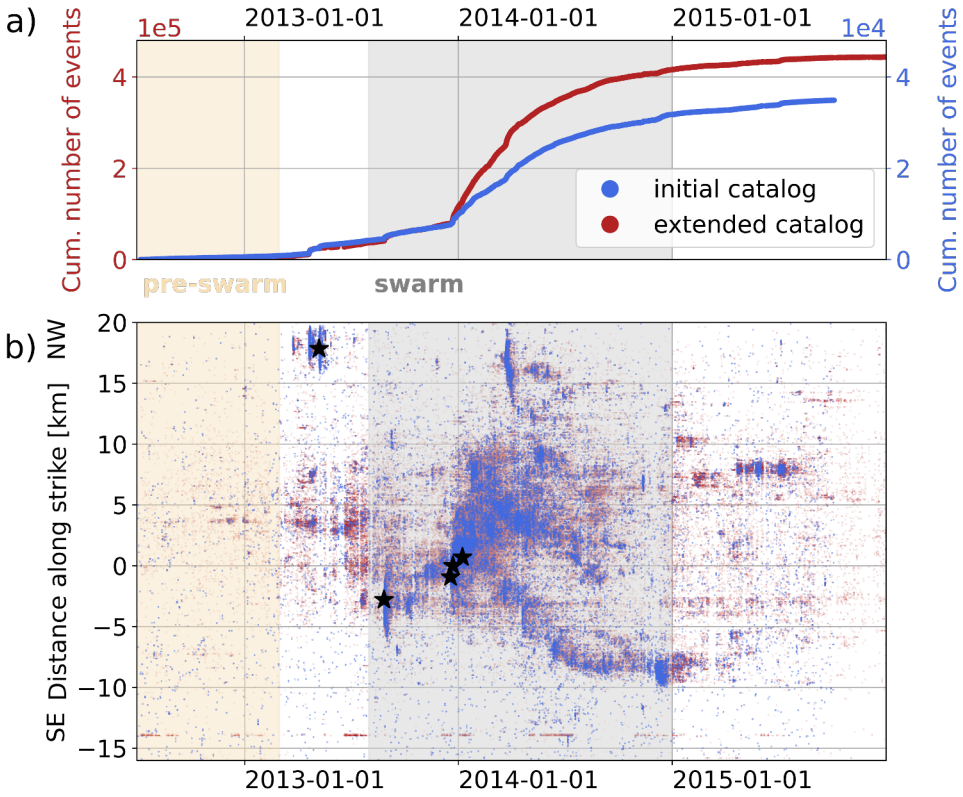

Figure 2: (a) Cumulative number of events for the initial (blue) and the extended (red) catalog. Note the two different scales. Two distinct time periods (pre-swarm and swarm) of distinctive style of seismicity are indicated. (b) Space-time evolution along strike for the initial (blue) and the extended (red) catalog. Black stars mark the five largest events within the study period (see Fig. 1).

3 The extended seismic catalog

From 28,903 templates we were able to retrieve 447,834 events, which time and space evolution is reported in figure 2, together with the initial catalog (Valoroso et al., 2017). The extended catalog contains one order of magnitude more events than the initial one while it preserves a similar time evolution for the cumulative number of events (Fig. 2a). This is seen as a first order quality estimate, as it reproduces the overall evolution of the seismicity.

An interesting feature of the extended catalog is that the detection increment factor is not constant during the studied period. In the first phase of the study (up to December 2013; Fig. 2a) we observe that the two catalogs follow the same time evolution even though the extended catalog having 10 times more events with respect to the initial one. However, at the onset of a significant increase of seismicity in January 2014, despite the time evolution remains similar, the increment factor exceeds 12 (Fig. 2a). To ensure that this evolution of event number is not related to changes in data quality we inspected the continuous data without finding anomalies. This increment is thus reflecting a true seismicity increase. Indeed, the extended catalog has a potential time resolution below 1.2 s, which allows to resolve events with short interevent times of less than 2 s interevent times (Fig. S1; Fig. S2). This factor is strongly influencing the increment factor we obtained, which allows to resolve an extremely high seismicity rate (e.g., January 2014, Fig. 2), and therefore enables the capture of its small-scale spatio-temporal dynamics.

We further observe 4,157 periodically activated events (Fig. S3a) at along strike distance approximately −15 km (Fig. 2b) within the extended catalog. These events were detected by templates located at shallow depths (between 0.09 to 1.9 km) within a small region at the southern end of the Gubbio basin close to a cement factory. The waveforms of these events (Fig. S3b) consist mainly of low frequency signals similar to the events observed by Latorre et al. (2014).

In the following analysis of our work, we removed these events, as they can be considered as a nuisance for earthquake related studies (Gulia & Gasperini, 2021). However, the dense report of human made signals can potentially be used to monitor changes in physical properties in the fault system, using recently proposed correlation approaches (Pinzon-Rincon et al., 2021).

In figure 3a we compare the frequency-magnitude distribution of the extended and the initial catalog (Valoroso et al., 2017). Despite we see a similar b-value (1) for both catalogs, the estimated magnitude of completeness (Herrmann & Marzocchi, 2021) decreased from 0.39 for the initial catalog to -0.67 for the extended one (Fig. 3a).

Figure 3b further compares the estimated magnitudes with the magnitudes of the initial catalog as a function of time. This figure again reveals the improved magnitude resolution of the extended catalog, and its capability to resolve in detail the large number of events associated with each burst of seismicity (Fig. 3b inset). There is however in both catalogs a daily evolution of minimum resolved magnitude, with smaller magnitude events better detected during nighttime (Fig. 3b inset). This phenomenon was already seen in another TM study (Sánchez-Reyes et al., 2021) and might be due to daily anthropogenic noise variation (Poli et al., 2020), and should be considered for example while performing statistical analysis of the seismicity (e.g., Marsan & Nalbant, 2005).

The results of the extended catalog can be partially compared with a previous study (Vuan et al., 2020), where the authors applied TM using events nucleating within 1,500 m from the assumed ATF surface to detect 16,000 earthquakes within our study period. With the TM approach presented here we are able to detect 32,158 events nucleating in the same fault volume, which corresponds to an extension factor > 2. We postulate that the reason for the improved performance in this study is related to the use of a higher frequency band and the higher sampling rate, which allows to better detect small magnitude events. Additionally, the borehole data used in this study seems to be less sensitive to noise (Chiaraluce et al., 2007), and therefore better resolve the micro-seismicity nucleated from the deeper parts of the LANF.

Even though we are able to detect a large amount of new seismic events from areas where templates are available, the inherent disadvantage of TM is its blindness for areas where no seismicity, or any other signal was previously identified. This represents the weak point of TM compared to other detection methods like used by Majstorović et al. (2021) which do not rely on previously characterized events from distinct areas. A further issue in the presented approach is the limitation to a borehole station network consisting of only 4 sensors (12 channels). During periods when no data is available for more than one station, the results of TM are less reliable, and are therefore not included within the extended catalog presented here. Especially during early 2013, Fig. 2c shows several gaps of data indicated by vertical empty lines.

The extended catalog is available in electronic format at https://www.dropbox.com/s/up3zq75wioimofk/cata_p
For each detected event we report the origin time, the position (which is the same as the template position), the estimated magnitude, the ID of the template detecting a given event (to group events into families) and the CC to MAD ratio. We further flag events which are human made. Different formats can be provided upon request to the authors.

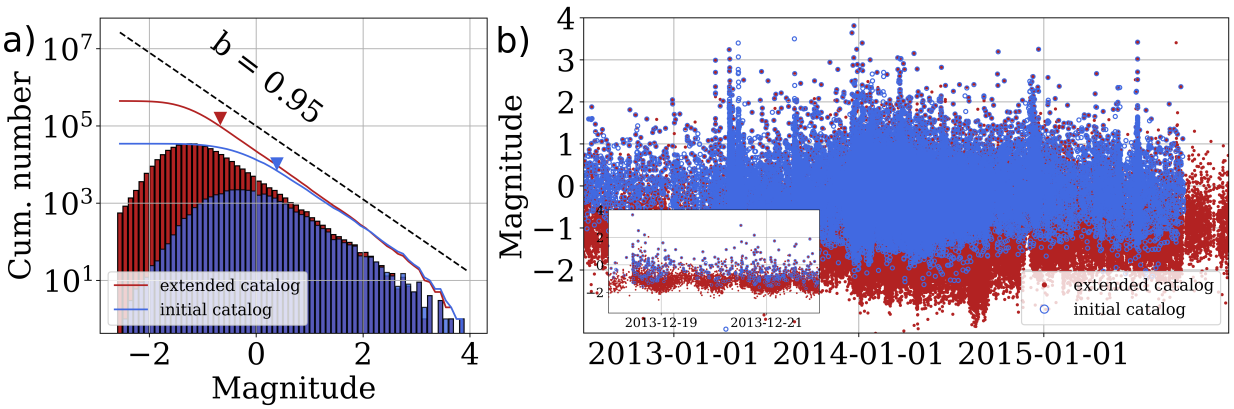

Figure 3: (a) Frequency-magnitude distribution for the initial (blue) and the extended (red) catalog. Continuous lines indicate the cumulative distributions. Dashed black line indicates the b-value of the initial catalog. Triangles indicate the magnitude of completeness estimated following the approach of Herrmann & Marzocchi (2021). (b) Magnitudes as a function of time for the initial (blue) and the extended (red) catalog. Inset: As (b) for a time period from 2013-12-18 until 2013-12-22.

4 Dynamics of the Seismicity

In the following, we use the extended catalog (without the 4,157 events which are most likely related to human induced sources) containing 443,677 events to derive new insights about the dynamics of the seismicity, to shed light on the deformation processes and infer the mechanical properties of the ATF fault system.

4.1 Time and space Clustering of the Seismicity

We start our analysis, by assessing the interaction in time and space between seismic events. Time and space clustering of earthquakes is commonly associated with interactions between events during co- and post-seismic processes, like static or dynamic stress transfer triggering (Freed, 2005) or afterslip (Perfettini & Avouac, 2004). Alternatively, enhanced interaction can result from external forcing as slow aseismic deformation (Frank et al. 2016; Lengliné et al., 2017; Poli et al., 2022), fluid fracturing (Obara, 2002; Seno & Yamasaki, 2003) or coupled fluid and rock interaction (Shelly et al., 2006).

We first divide the seismicity into pre-swarm (beginning of the catalog until 2013-03-01T00:00:00) and swarm (2013-08-01T00:00:00 until 2014-12-31T00:00:00) time periods (Fig. 2), guided by the results of Gualandi et al., (2017) and Valoroso et al. (2017). To assess the time and space interaction during these two periods, we discretize the seismicity in space into 1 km bins along depth. Then, for each bin we count the number of events occurring in each time bin of 1-hour.

We start by evaluating the spatial population dynamics (Bjørnstad et al., 1999), to retrieve synchronous populations of earthquakes. To that scope, we compute the zero-lag cross-correlation (ZCC) between the event count time series defined above (Fig. 4a, b). The resulting ZCC is expected to be high for time series having similar time evolution, thus indicating synchronous activation over different space bins (Bjørnstad et al., 1999; Frank et al., 2016; Trugman et al., 2015; Wu et al., 2015).

Figure 4a shows the results of our analysis, for the pre-swarm period. Here, small ZCC off the diagonal are observed for the full depth range, suggesting marginal spatial interaction. On the other hand, during the swarm period (Fig. 4b) there is a clear separation between two depth ranges. The shallow part above ~7 km depth exhibits large ZCC off the diagonal, indicating a significant synchronization and thus an elevated spatial interaction of the seismicity, while below ~7 km of depth, the seismicity exhibits small ZCC, similar to the values during the pre-swarm period (Fig. 4a).

Following the same approach, in in figure 4d and 4e, we show the spatiotemporal interaction using 1km bins along strike. We observe again a generalized marginal interaction of the pre-swarm seismicity (Fig. 4d), while significant synchronization is observed up to 5-10km, during the swarm period (Fig. 4e).

We further assess the time interaction of the seismicity along depth, considering a point process formalism (Lowen & Teich, 2005), and autocorrelations of the event count time series. If the auto-correlation function exhibits a distinct pulse at zero lag-time, the seismicity is temporally unrelated as expected for a Poisson process like random seismicity (Lowen & Teich, 2005). On the other hand, a smooth drop of the auto-correlation function at zero lag-time indicates an auto-regressive model, in which the time of future earthquakes is related to the previous ones (Lowen & Teich, 2005). Figure S4a shows the auto-correlation functions for the pre-swarm period. Here the pulse at zero lag-time indicates poissonian-like evolution of seismicity over the entire depth range. For the swarm period (Fig. S4b), we can distinguish between two types of behavior. The shallow part (above 7 km depth) where the auto-correlation function exhibits a smooth decay around zero lag-time, indicating a significant time interaction. On the other hand, for deeper parts (below 7 km) the auto-correlation functions show a distinct pulse, like seen for the entire depth range in the pre-swarm period (Fig. S4).

We also explore the time interaction of the seismicity occurring in each depth bin, by calculating the coefficient of variation (COV) (Fig. 4c). The COV provides insightful information about the time clustering of earthquakes (e.g., Cabrera et al. 2022; Kagan & Jackson, 1991; Sánchez-Reyes et al. 2021; Schoenball & Ellsworth, 2017). A COV of ~1 indicates a Poissonian distribution of the interevent times while a COV » 1 indicates temporal clustering, indicative of high interaction between events. Note that for this step we release the time binning applied in the approach before but use the interevent time of events in different depth bins, thus exploring the time clustering at time scales even

smaller than one hour.

Figure 4 c) shows the COV over the depth bins for the pre-swarm period (blue line) and the swarm period (red line). The pre-swarm period exhibits quasi stable values for the COV (< 2) over the entire depth range. For the swarm period again, we can distinguish between two different regimes. The shallow part (above 7 km depth) exhibits COV > 2 indicating elevated interaction in time. At deeper parts (below 7 km depth) of the study area the COV drops to pre-swarm values.

The results from the spatial-temporal analysis discussed above suggest that i) seismicity exhibits strong space (Fig. 4) and time (Fig. 4c, S4) interaction mainly occurring during the swarm period and ii) during the swarm, there exists a decoupled style of seismicity in between the shallow and deeper (> 7km) part of the fault system.

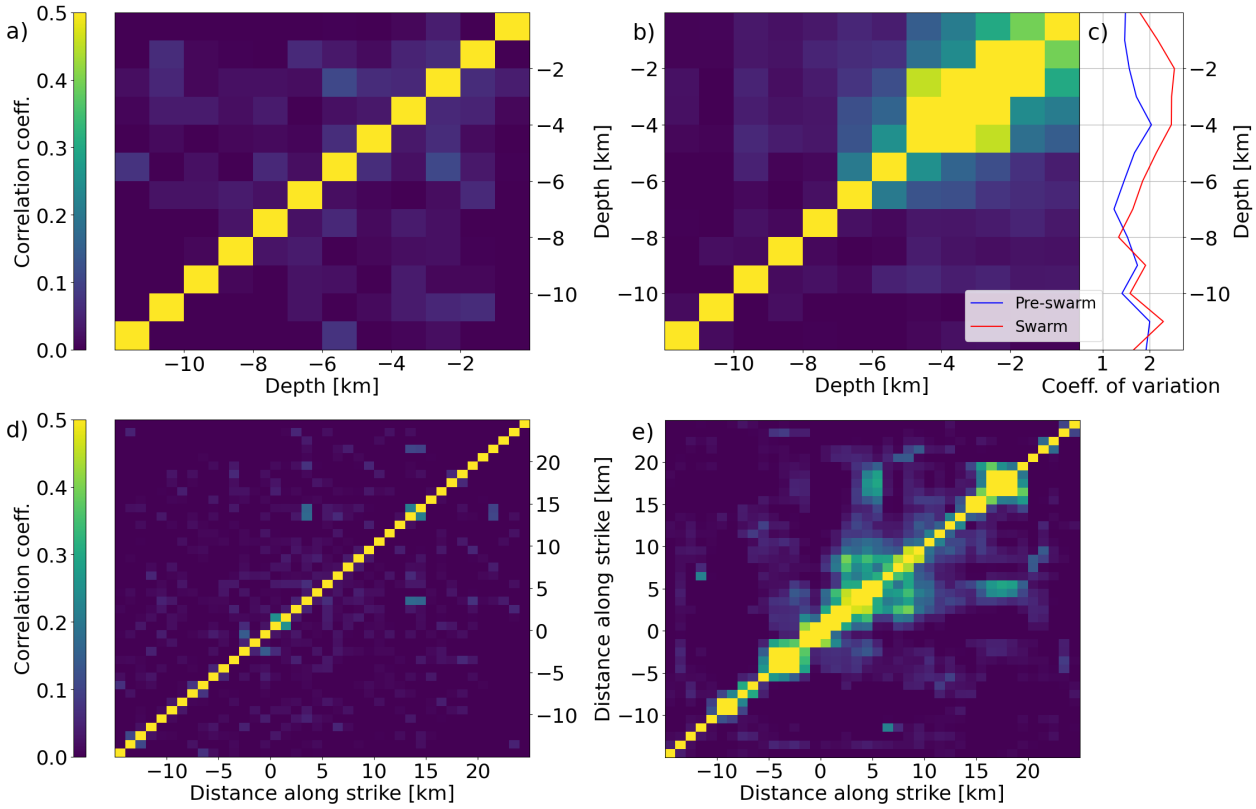

Figure 4: Pairwise correlation coefficients between the event count time series binned in 1 km along depth and 1-hour lasting time bins for (a) the pre-swarm and (b) the swarm time period. For both plots, the color-bar ranges from 0 to 0.5. (c) Coefficient of variation of the inter-event times for 1 km depth bins for the pre-swarm (blue) and the swarm (red) period. (d) Pairwise correlation

coefficients between the event count time series binned in 1 km along strike and 1-hour lasting time bins for the pre-swarm and (e) the swarm time period. For both plots, the color-bar ranges from 0 to 0.5.

4.2 Temporal behavior of template families

We further focus on the characteristics of event families. Similar to previous studies (e.g., Cochran et al., 2018; Shelly & Johnson, 2011), a family is defined as a group of detections related to the detecting template. From figure 1c it is visible that waveforms within a family share similar features with their template, indicating qualitatively the proximity of the events belonging to a particular family. To quantify distances between events within a family, we take advantage of the redundant events reported in section. 2. We consider events which were used as templates, and at the same time detected by other templates. As for these events we know the precise location, we can calculate the hypo-central distances between the location of the auto-detection (i.e., a template detects the event which it was extracted from) and the locations of all additional templates, which detected this particular event. From the distances we obtain an approximation of the expected hypo-central distances between a mother event and other events within the former defined families. We perform this analysis for 2,052 cases of redundant detections which corresponds to ~5% of the catalog (Fig. S5). In figure S5 we observe that most redundant events have a hypo-central distance of ~250m to the auto-detection. We therefore assume that hypo-central distances between events within a family can be expected to be approximately equal to that value. This leads us to the consideration that a family of events allows us to probe the time evolution of asperities that are close to each other, in a localized zone of the fault (e.g., Cochran et al., 2018).

Guided from the results of section 4.1, we divide the families into shallow and deep families, using a depth threshold of 7 km. For each family, we estimate the interevent times and normalize them by the total duration of each family. The resulting normalized interevent times ( ) are then sorted within logarithmic time bins and counted. We account for logarithmic spacing, by dividing the number of normalized interevent times per bin by the length of the bin and the total number of normalized interevent times (Duverger et al., 2018). This processing provides the distributions of the interevent times for the two different depths, plotted in figure 5a. Their general shape can be described with a truncated gamma function:

$$\rho(\tau) = C(\tau)^{\gamma-1} \cdot e^{-\frac{\tau}{\beta}} \quad (1)$$

where C and are constant while indicates the time clustering of the seismicity (Hainzl et al., 2006). For $\gamma = 1$ the seismicity is Poissonian and occurs randomly in time, while for $\gamma = 0$ it follows a power-law decay similar to an Omori-like sequence (Duverger et al., 2018; Omori, 1894; Poli et al., 2022).

For families of the shallow part (above 7 km depth; Fig. 5a) the logarithmic interevent time linearly decays over four orders of time magnitude and can be fitted (eq. 1) with $\gamma \sim 0.26$. This value of γ is indicative of seismicity

clustered in time (Duverger et al., 2018; Poli et al., 2021), but differs from classic aftershock sequence (e.g., Omori, 1894).

For the deep families (below 7 km depth; Fig. 5a) we observe a clear change of the slope at $\tau \sim 10e{-}2$. This change of slope is indicative of a bi-modal behavior of the seismicity, similarly to the observations of Thomas et al. (2018) for low frequency earthquakes (LFE). More in particular, for small τ ($\tau < 10e-2$) the distribution decays with $\gamma = 0$, indicative of an Omori-like process (Omori, 1894). On the other hand, for $\tau > 10e-2$ the seismicity becomes less time clustered, with $\gamma = 0.55$.

To visualize the behavior of distinct time clustering discussed above, in figure 5b, c, d we show the cumulative number as function of time, for the deep and shallow seismicity. For deep seismicity with short interevent time intervals of less than 10^4s (Fig. 5b), we clearly see that the time clustering observed in figure 5a, is mainly associated with intermittent occurrence of rapid bursts of seismicity. In contrast to that, the seismicity with long interevent time intervals (> 10^5s) evolves with a nearly constant rate for the whole duration of our study period (Fig. 5c). The seismicity related to shallow families after the increment of events in January 2014 fades out over time by following an Omori-like decay, without however being governed by a large mainshock (Fig. 5d), as observed for other swarms (Poli et al., 2022).

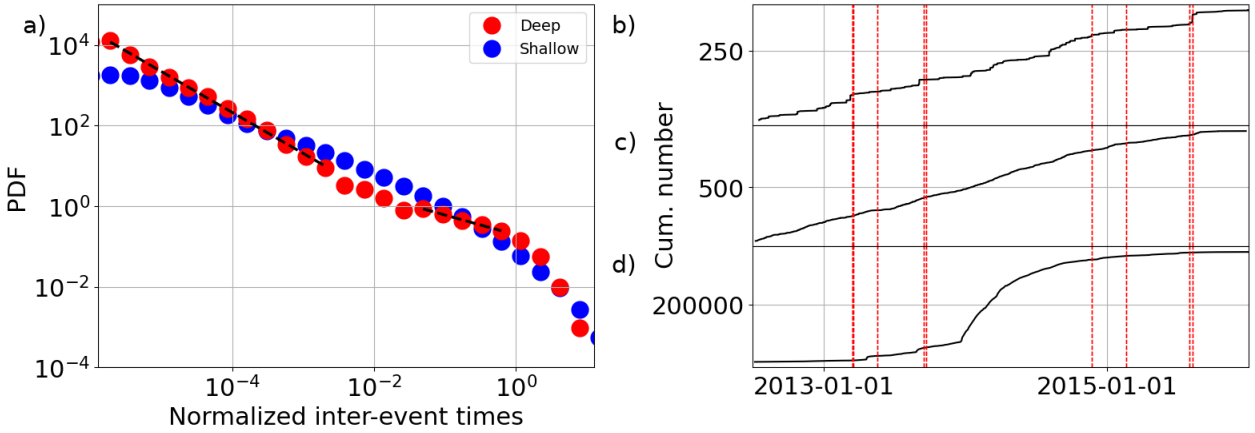

Figure 5: (a) Probability density function for the normalized inter-event times of deep (red) and shallow (blue) template families. Dashed black line indicate the least squares polynomial fit for the indicated areas. (b) Cumulative number for events with short interevent time intervals (<10^4 s) until the next event in the deep part. Vertical red dashed lines indicate the origin times of repeating events. (c) As (b) but for long interevent time intervals (> 10^5 s) until the next event. (d) As (b) but for events within the shallow part.

4.3 Repeating Earthquakes along the LANF

One of the proposed mechanisms to explain the accommodation of the exten-

sion within the study area is constant creep along the LANF (Anderlini et al., 2016; Vadacca et al., 2016). Creeping faults are well known to generate repeating earthquakes: earthquakes highly similar in terms of waveforms, frequently radiated from a single asperity which is constantly brought to failure due to constant loading in the surrounding area (Nadeau & McEvilly, 1999).

In this work, we systematically search for repeating earthquakes along the LANF as evidence of creep, by correlating the waveforms of events occurring below 7 km depth. To that scope, we follow the approach of Duverger et al. (2018) and estimate the similarity value between event pairs over the entire station network, while considering the SNR of each component. We limit our analysis only on waveform similarities, without any attempt to relocate highly similar events (Uchida & Bürgmann, 2019).

For each pair of events with a hypo-central distance of less than 750 m in between, we extract the waveforms on all 12 components and cut it into 9.5 seconds lasting windows (sampled at 500 Hz) starting with the p-arrival and including substantial portions of the s-coda (Fig. 6a inset). The waveforms are filtered between 1.5 and 15 Hz. For every detection we estimate the SNR within a 0.5 second lasting window before the P-arrival. We cross-correlate the waveforms component-wise and extract the maximum of the resulting cross-correlation function. This maximum is then averaged over the station network while values extracted from components with a low SNR are down weighted with a logistic function (Duverger et al., 2018; supplementary material).

Next, we group events sharing a similarity value (> 0.95) following a simple equivalence class approach (i.e., if event A and B share a high similarity value, they open a family, if an additional event C shares a high similarity value with only one of the events A or B, it is grouped into that family).

This approach leads to 10 event families of repeating events (Fig. 6; Tab. S2). The majority of these families consist of two events (doublets), in agreement with previous studies (Valoroso et al., 2017), while only two families consist of 3 events (Tab. S2). The obtained families are all characterized by short durations ranging from seconds to several hours (Fig. 6b; Tab. S2). Additionally, from figure 5d it is clear that families occur unrelated to the starting time of the swarm-like seismic sequence in the shallow part of the HW, while some of them seem to be correlated in time with the short duration bursts observed from the short-lasting template families (Fig. 5b).

The short duration of all families implies short interevent times and therefore seems to suggest that the observed events are not governed by fault creep (Hatch et al., 2020). To corroborate this hypothesis, we define the repeating earthquakes rate (R) to be controlled by the slip rate (V) on the surrounding fault:

$$R = \frac{V}{D} \quad (2)$$

where D is the characteristic slip per event (Thomas et al., 2018). We combine the moment ($M_0 = \mu AD$) and assume the stress drop σ defined according to

Madariaga (1976) for a circular crack with area $A = \pi * r^2$, to obtain:

$$D = \frac{M_0}{\mu * \pi * \left(\frac{7M_0}{16\sigma}\right)^{\frac{2}{3}}} \quad (3)$$

We here assume σ of 3 MPa (Chiaraluce et al., 2007), μ of 30 GPa, and a creep rate V of 1.7 mm/yr, as proposed by Anderlini et al. (2016). We then compute the expected event rate as a function of the seismic moment (Fig. 6b). The observed interevent times are 2-3 orders of magnitude smaller than the expected interevent times for constant creep of 1.7 mm/yr (Anderlini et al., 2016), suggesting that the events observed along the LANF are not driven by creep.

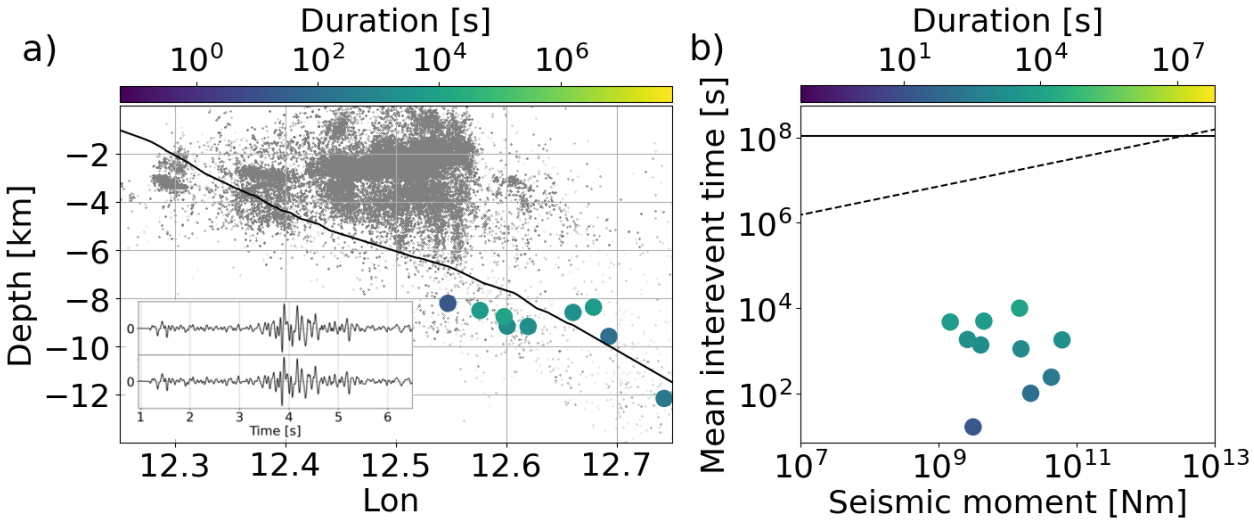

Figure 6: (a) Cross section of the ATF. Grey dots indicate the overall seismicity while the LANF model is indicated as a black line. Color-coded dots indicate the locations and the duration of the found repeating event families. (b) Mean interevent times as a function of seismic moment. Black dashed line indicates the interevent times expected for a loading rate of 1.7 mm/yr. Black solid line indicates the whole time of the study period. Color-coded dots as in (a).

5 Discussion

The presented analysis reveals different modes of seismicity in different parts of the ATF fault system, which can be summarized as: i) the shallow seismicity (depth $<$ 7km), occurring along syn- and antithetic high angle normal faults (Piana Agostinetti et al., 2017; Valoroso et al., 2017) during the transient aseismic deformation process (Gualandi et al., 2017), is strongly clustered in time and space (Fig. 4 and 5), ii) deep seismicity (depth $>$ 7km) including the LANF exhibits only marginal time and space clustering (Fig. 4; Fig. 5), and is characterized by a bimodal time evolution, with short time-clustered (Fig. 5b) and long and non-time clustered (Fig. 5c) seismicity. We now discuss in more details

the different types of seismicity and the possible physical processes governing them.

5.1 The Shallow Seismicity

The shallow seismicity (depth < 7km) is mainly radiated by the syn- and antithetic high angle normal faults, which stand above the LANF (Gualandi et al., 2016; Valoroso et al., 2017). This shallow seismicity is showing a significant spatial clustering, which implies a simultaneous activation of large fault portions (up to 4 km along depth, 5 to 10 km along strike) over the time scale of 1 hour (Fig. 4b, e). The spatial interaction observed is accompanied by a significant increment of time clustering (Fig. 4c; Fig. S4b). However, the clustering is occurring only during the aseismic deformation episode observed by Gualandi et al., (2017). The analysis of the interevent times (Fig. 5a) and the time evolution of cumulative events (Fig. 5d) reveal that the swarm seismicity evolves in time like an Omori-like sequence, but the lack of a clear mainshock and the $\gamma \sim 0.26$, obtained from eq. 1, do not support the hypothesis of stress transfer from large events to govern the evolution of the seismicity (Duverger et al., 2018; Poli et al., 2022).

The observation of time and space clustering indicates that the occurrence of future events is controlled by previous ones (Beaucé et al., 2019). This behavior is often related to elastic interaction (Freed, 2005), where the complexity of a fault system is likely controlling the interaction of earthquakes (Kato et al., 2021; Scholz, 2019). Alternatively, time and space relations can be linked to the complexity of different physical process, like aseismic slip (Frank et al., 2016; Lengliné et al., 2017), fluid fracturing (Obara, 2002; Seno & Yamasaki, 2003) or a coupled system of fluid and rock interaction (Shelly et al., 2006).

A mechanism explaining the rapid (1 hour) synchronization of seismicity in large parts (up to 5km) of the fault (Fig. 4) could be stress transfer from large events (Freed, 2005). However, the space synchronization of seismicity is up to 5km, that is ~30 times larger than the fault size for the largest events in the sequence. Moreover, the synchronization observed in figure 4 is not always occurring close to these large events.

We alternatively propose that the increment of time and space clustering observed during the transient aseismic deformation signal (Gualandi et al., 2017), is mainly a by-product of aseismic slip, with additional elastic interaction, which plays a significant role even for small magnitude seismicity (Helmstetter et al., 2005). Thus, the evolution of the seismicity resembles to the behavior of LFEs observed in subduction or transform faults, during slow slip events (Frank et al., 2016; Tan & Marsan, 2020). With this model, the seismicity can directly be used to assess the fine spatio-temporal evolution of transient aseismic slip, not resolvable by daily geodetic measurements (Gualandi et al., 2017). Our interpretation further implies that the reported transient aseismic deformation is similar to the one observed in subduction zones. In the study area the different rheology of the shallow normal faults (Piana Agostinetti et al., 2017), as well as

lower temperature and pressure values do not permit the occurrence of tremors or LFE, but rather of regular seismicity.

The strong interactions observed (Fig. 4; Fig. S4), also suggest the complexity of the fault system, which is likely to consist of groups of asperities along large faults, or complex fracture networks in a fault volume. In both cases, the resulting effective rheology is likely to inhibit the propagation of large magnitude earthquakes in the shallow syn- and antithetic faults.

We finally highlight how the lack of interaction (Fig. 4; Fig. S4), in periods outside the time of the transient aseismic deformation, indicates a mostly coupled fault system within the shallow part.

5.2 The Deep Seismicity

A clear change of the seismicity is observed at depths below 7 km, where spatial (Fig. 4) and temporal interaction (Fig. S4) are no longer observed, even during the transient aseismic deformation episode in 2014 (Gualandi et al., 2017). This observation indicates that the deeper part of the LANF is not activated during the transient aseismic deformation episode (Gualandi et al., 2017), differently from what was discussed by Vuan et al. (2020).

We further observe that the deep seismicity follows a bimodal time evolution, with rapid reoccurring events (<10^4 s) having a significant temporal interaction (Fig. 5a, b), while the long-lasting reoccurring events (> 10^5 s) exhibiting a nearly constant time evolution (Fig. 5a, c).

The systematic analysis of waveforms similarity permitted to discovered 10 groups of repeating earthquakes. These events are used to understand the role of creep along the ATF (Anderlini et al., 2016). To corroborate the role of creep we use a simple creep model driving the rupture of asperities (sec. 4.3). With this model the interevent times of the repeating events are incompatible with creep observed with geodetic data (Anderlini et al., 2016; Fig. 6). One can argue that given the small tectonic loading rate, the study period is too short to resolve any repeating earthquake sequence. However, the expected interevent time for small magnitude repeating earthquake sequence is well below the duration of the extended catalog (Fig. 6b), enabling the observation of creep related REs, unless the LANF events are characterized by an extremely small stress drop, two orders of magnitude smaller than the assumed stress drop of 3MPa.

The style of the repeating earthquakes is more similar to the mentioned short-lasting families (Fig. 5a, b), with duration of the order of up to a few hours, also observed by Valoroso et al., (2017). The driving mechanism for this rapidly repeaters could therefore be stress transfer on close asperities (Chen et al., 2013; Lengliné & Marsan, 2009). However, by analyzing the position of the largest events within each repeating earthquakes family, we did not recognize any clear mainshock aftershock behavior (Fig. S6).

The rapid recurrence of repeating events could be linked to the significant amount high pore-fluid pressure observed in the ATF fault system (Piana

Agostinetti et al., 2017). Following the model of Baisch & Harjes (2003), multiple failure of the same asperity can occur for an increase of fluid pressure. The repeating events (Fig. 6), can thus represent a mode of rupture, fully driven by short lasting (10-1000s) pore pressure changes, as suggested by Collettini (2002). A simplified calculation of the pore pressure change can be done by dividing the cumulative stress drop for each repeating earthquake family and assuming a coefficient of friction of 0.6 (Baisch & Harjes 2003). For a stress drop of 3 Mpa, we obtain 10-15 MPa of pore pressure change over times ranging from ~10-1000s.

Together with the short bursts of events discussed above, we observe the occurrence of the long term and nearly continuous seismicity observed along the LANF at depth > 7km (Fig. 5c). Without any clear spatial and temporal clustering (Fig. 4; Fig 5a, c), this seismicity might reflect continuous deformation similar to creep proposed by Anderlini et al., (2016). However, here creep is not accompanied by long-lasting repeating earthquakes (Fig. 6), as in other creeping faults (e.g., Nadeau & McEvilly, 1999). One possible explanation is that the rheological conditions on the LANF are different compared to creeping strike slip faults or subduction zones (e.g., Nadeau & McEvilly, 1999; Uchida & Bürgmann, 2019). This hypothesis is however in contrast with geological studies, which describe the ATF as composed of a continuously deforming ductile matrix, with embedded lens of competent material, which represents seismically active asperities (Collettini et al., 2011).

In an alternative model the deformation across the ATF system observed geodetically at the surface (Anderlini et al., 2016), can be understood assuming an effective opening of a non-elastic volume at depth (D'Agostino & D'Anastasio, 2012), like the one proposed for the Gulf of Corinth (Lambotte et al., 2014). This volume can represent the effect of over-pressurized CO2 rising form the mantle, sealed below the LANF (Chiodini et al., 2004). For this model, no creep is needed, in agreement with our observations. In this case the continuous seismicity observed along the LANF (Fig. 1a; Fig 5c) is resulting from strain below the central part of the LANF (Lambotte et al., 2014). This last discussion calls for novel seismo-geodetic analysis to better understand the deformation style along the LANF.

6 Conclusion

By applying TM processing (Beaucé et al., 2018; Gibbons & Ringdal, 2006) to data recorded at an array of borehole stations we were able to produce a catalog of 443,677 earthquakes, expanding by 12 times the number of events within the initial catalog (Valoroso et al., 2017). The new seismic catalog is complete to magnitude down to -0.67.

While TM is powerful to detect many more events, with low SNR, no objective method can be used to define a good and time consistent detection threshold. We therefore performed several quality controls on the detected signals to ensure to have a minimal impact of false detections in the extended catalog. With

the presented approach we significantly improved the detection of small events, being able to detect earthquakes with magnitude as low as −2 (Fig. 3). An electronic format of the extended catalog can be accessed at https://www.dropbox.com/s/up3zq75wioimofk/cata_pub.txt?dl=0.

The detailed analysis of this catalog permitted to reveal different styles of seismicity in different times and fault regions. We first observe marginal time and space clustering during periods not affected by aseismic deformation, along the full fault system (Fig. 4a, d; Fig. S4a). On the other hand, in concomitance with the 2014 aseismic deformation episode (Gualandi et al., 2017), the shallow seismicity starts to be strongly clustered in time and space. We propose that this enhanced interaction of seismicity reflects the complexity of slip process during the transient.

In the deeper part of the fault system (>7km), along the ATF, we observe bimodal seismicity (Fig. 5), with long and nearly continuous families of events, and short bursts with duration less than 1 day. We further detect and model repeating earthquakes and illustrate the marginal role of creep in controlling their occurrence (Fig. 6). We thus proposed rapid changes of pore pressure as driver for rapid repeating events, in agreement with geological studies (Collettini, 2002).

The lack of clear seismological evidence for creep along the ATF calls for more detailed seismo-geodetic studies to better assess the deformation style occurring along the ATF during the inter-seismic period (Anderlini et al., 2016; Vadacca et al., 2016).

7 Data and Resources

During the review process, the catalog can be downloaded via https://www.dropbox.com/s/up3zq75wioimofk/ca
The continuous seismic data used in this study are available at the Istituto Nazionale di Geofisica e Vulcanologia (INGV) seismological data center (http://cnt.rm.ingv.it/webservices_and_software/, last accessed May 2021) and were downloaded using obspyDMT (Hosseini & Sigloch, 2017). For data processing we made us of the ObsPy package (Beyreuther et al., 2010; Krischer et al., 2015). The fast matched filter code was used for template matching (Beaucé et al., 2018). Computations were performed using the University of Grenoble Alpes (UGA) High-Performance Computing infrastructures CIMENT. Maps were created using the Generic Mapping Tools (GMT) version 6.0 and PyGMT (Uieda et al., 2021). Supplemental material for this article contains six figures, two tables and one equation, expanding the information presented in this manuscript.

Declaration of Competing Interest

The authors acknowledge there are no conflicts of interest recorded.

Acknowledgments

This research received funding from the European Research Council (ERC)

under the European Union Horizon 2020 Research and Innovation Program (grant agreements 802777- MONIFAULTS). The authors acknowledge Glenn Cougoulat and GRICAD Grenoble Alpe Research - Scientific Computing and Data Infrastructure for their kind support during the computational part of this work.

References

Abercrombie, R. E. (2021). Resolution and uncertainties in estimates of earthquake stress drop and energy release. Philosophical Transactions of the Royal Society A, 379(2196), 20200131.

Abers, G. A., Mutter, C. Z., & Fang, J. (1997). Shallow dips of normal faults during rapid extension: Earthquakes in the Woodlark-D'Entrecasteaux rift system, Papua New Guinea. Journal of Geophysical Research: Solid Earth, 102(B7), 15301-15317.

Anderlini, L., Serpelloni, E., & Belardinelli, M. E. (2016). Creep and locking of a low-angle normal fault: Insights from the Altotiberina fault in the northern Apennines (Italy). Geophysical Research Letters, 43(9), 4321-4329.

Baisch, S., & Harjes, H. P. (2003). A model for fluid-injection-induced seismicity at the KTB, Germany. Geophysical Journal International, 152(1), 160-170.

Barchi, M., Minelli, G., Magnani, B., & Mazzotti, A. (2003). Line CROP 03: Northern Apennines. Mem. Descr. Carta Geol. d'Italia LXII, 62, 127-136.

Beaucé, E., Frank, W. B., & Romanenko, A. (2018). Fast matched filter (FMF): An efficient seismic matched-filter search for both CPU and GPU architectures. Seismological Research Letters, 89(1), 165-172.

Beaucé, E., Frank, W. B., Paul, A., Campillo, M., & van der Hilst, R. D. (2019). Systematic detection of clustered seismicity beneath the Southwestern Alps. Journal of Geophysical Research: Solid Earth, 124(11), 11531-11548.

Beyreuther, M., Barsch, R., Krischer, L., Megies, T., Behr, Y., & Wassermann, J. (2010). ObsPy: A Python toolbox for seismology. Seismological Research Letters, 81(3), 530-533.

Biemiller, J., Boulton, C., Wallace, L., Ellis, S., Little, T., Mizera, M., ... & Lavier, L. (2020). Mechanical implications of creep and partial coupling on the world's fastest slipping low-angle normal fault in southeastern Papua New Guinea. Journal of Geophysical Research: Solid Earth, 125(10), e2020JB020117.

Bjørnstad, Ottar N., Rolf A. Ims, and Xavier Lambin. "Spatial population dynamics: analyzing patterns and processes of population synchrony." *Trends in Ecology & Evolution* 14.11 (1999): 427-432.

Boncio, P., Brozzetti, F., & Lavecchia, G. (2000). Architecture and seismotectonics of a regional low-angle normal fault zone in central Italy. Tectonics, 19(6), 1038-1055.

Byerlee, J. (1978). Friction of rocks. In *Rock friction and earthquake prediction* (pp. 615-626). Birkhäuser, Basel.

Cabrera, L., Poli, P., & Frank, W. B. (2022). Tracking the Spatio-Temporal Evolution of Foreshocks Preceding the Mw 6.1 2009 L'Aquila Earthquake. Journal of Geophysical Research: Solid Earth, 127(3), e2021JB023888.

Chen, K. H., Bürgmann, R., & Nadeau, R. M. (2013). Do earthquakes talk to each other? Triggering and interaction of repeating sequences at Parkfield. Journal of Geophysical Research: Solid Earth, 118(1), 165-182.

Chiarabba, C., & Amato, A. (2003). Vp and Vp/Vs images in the Mw 6.0 Colfiorito fault region (central Italy): A contribution to the understanding of seismotectonic and seismogenic processes. Journal of Geophysical Research: Solid Earth, 108(B5).

Chiaraluce, L., Chiarabba, C., Collettini, C., Piccinini, D., & Cocco, M. (2007). Architecture and mechanics of an active low-angle normal fault: Alto Tiberina fault, northern Apennines, Italy. Journal of Geophysical Research: Solid Earth, 112(B10).

Chiaraluce, L., Amato, A., Carannante, S., Castelli, V., Cattaneo, M., Cocco, M., ... & Valoroso, L. (2014). The Alto Tiberina Near Fault Observatory (northern Apennines, Italy). Annals of Geophysics.

Chiodini, G., Cardellini, C., Amato, A., Boschi, E., Caliro, S., Frondini, F., & Ventura, G. (2004). Carbon dioxide Earth degassing and seismogenesis in central and southern Italy. Geophysical Research Letters, 31(7).

Cochran, E. S., Ross, Z. E., Harrington, R. M., Dougherty, S. L., & Rubinstein, J. L. (2018). Induced earthquake families reveal distinctive evolutionary patterns near disposal wells. Journal of Geophysical Research: Solid Earth, 123(9), 8045-8055.

Collettini, C. (2002). Hypothesis for the mechanics and seismic behaviour of low-angle normal faults: the example of the Altotiberina fault Northern Apennines. Annals of Geophysics, 45(5).

Collettini, C. (2011). The mechanical paradox of low-angle normal faults: Current understanding and open questions. *Tectonophysics*, *510*(3-4), 253-268.

Collettini, C., & Barchi, M. R. (2002). A low-angle normal fault in the Umbria region (Central Italy): a mechanical model for the related microseismicity. Tectonophysics, 359(1-2), 97-115.

Collettini, C., Niemeijer, A., Viti, C., Smith, S. A., & Marone, C. (2011). Fault structure, frictional properties and mixed-mode fault slip behavior. Earth and Planetary Science Letters, 311(3-4), 316-327.

D'Agostino, N., & D'Anastasio, E. (2012, December). Negative geodetic evidence for active aseismic creep on low-angle normal faults in the Umbria-Marche Apennines (Italy). In AGU Fall Meeting Abstracts (Vol. 2012, pp. G23B-0914).

Duverger, C., Lambotte, S., Bernard, P., Lyon-Caen, H., Deschamps, A., & Nercessian, A. (2018). Dynamics of microseismicity and its relationship with the active structures in the western Corinth Rift (Greece). Geophysical Journal International, 215(1), 196-221.

Frank, W. B., Shapiro, N. M., Husker, A. L., Kostoglodov, V., Gusev, A. A., & Campillo, M. (2016). The evolving interaction of low-frequency earthquakes during transient slip. Science advances, 2(4), e1501616.

Frank, W. B., Rousset, B., Lasserre, C., & Campillo, M. (2018). Revealing the cluster of slow transients behind a large slow slip event. Science advances, 4(5), eaat0661.

Freed, A. M. (2005). Earthquake triggering by static, dynamic, and postseismic stress transfer. Annu. Rev. Earth Planet. Sci., 33, 335-367.

Gibbons, S. J., & Ringdal, F. (2006). The detection of low magnitude seismic events using array-based waveform correlation. Geophysical Journal International, 165(1), 149-166.

Gualandi, A., Nichele, C., Serpelloni, E., Chiaraluce, L., Anderlini, L., Latorre, D., ... & Avouac, J. P. (2017). Aseismic deformation associated with an earthquake swarm in the northern Apennines (Italy). Geophysical Research Letters, 44(15), 7706-7714.

Gulia, L., & Gasperini, P. (2021). Contamination of Frequency–Magnitude Slope (b-Value) by Quarry Blasts: An Example for Italy. Seismological Society of America, 92(6), 3538-3551.

Hainzl, S., Scherbaum, F., & Beauval, C. (2006). Estimating background activity based on interevent-time distribution. Bulletin of the Seismological Society of America, 96(1), 313-320.

Hatch, R. L., Abercrombie, R. E., Ruhl, C. J., & Smith, K. D. (2020). Evidence of aseismic and fluid-driven processes in a small complex seismic swarm near Virginia City, Nevada. Geophysical Research Letters, 47(4), e2019GL085477.

Helmstetter, A., Kagan, Y. Y., & Jackson, D. D. (2005). Importance of small earthquakes for stress transfers and earthquake triggering. Journal of Geophysical Research: Solid Earth, 110(B5).

Herrmann, M., & Marzocchi, W. (2021). Inconsistencies and lurking pitfalls in the magnitude–frequency distribution of high-resolution earthquake catalogs. Seismological Research Letters, 92(2A), 909-922.

Hosseini, K., & Sigloch, K. (2017). ObspyDMT: a Python toolbox for retrieving and processing large seismological data sets. Solid Earth, 8(5), 1047-1070.

Hreinsdóttir, S., & Bennett, R. A. (2009). Active aseismic creep on the Alto Tiberina low-angle normal fault, Italy. Geology, 37(8), 683-686.

Kagan, Y. Y., & Jackson, D. D. (1991). Long-term earthquake clustering. Geophysical Journal International, 104(1), 117-133.

Kato, A., Sakai, S. I., Matsumoto, S., & Iio, Y. (2021). Conjugate faulting and structural complexity on the young fault system associated with the 2000 Tottori earthquake. Communications Earth & Environment, 2(1), 1-9.

Krischer, L., Megies, T., Barsch, R., Beyreuther, M., Lecocq, T., Caudron, C., & Wassermann, J. (2015). ObsPy: A bridge for seismology into the scientific Python ecosystem. Computational Science & Discovery, 8(1), 014003.

Lambotte, S., Lyon-Caen, H., Bernard, P., Deschamps, A., Patau, G., Nercessian, A., ... & Adamova, P. (2014). Reassessment of the rifting process in the Western Corinth Rift from relocated seismicity. Geophysical Journal International, 197(3), 1822-1844.

Latorre, D., Amato, A., Cattaneo, M., Carannante, S., & Michelini, A. (2014). Man-induced low-frequency seismic events in Italy. Geophysical Research Letters, 41(23), 8261-8268.

Lengliné, O., & Marsan, D. (2009). Inferring the coseismic and postseismic stress changes caused by the 2004 Mw= 6 Parkfield earthquake from variations of recurrence times of microearthquakes. Journal of Geophysical Research: Solid Earth, 114(B10).

Lengliné, O., Frank, W. B., Marsan, D., & Ampuero, J. P. (2017). Imbricated slip rate processes during slow slip transients imaged by low-frequency earthquakes. Earth and Planetary Science Letters, 476, 122-131.

Lowen, S. B., & Teich, M. C. (2005). Fractal-based point processes. John Wiley & Sons.

Madariaga, R. (1976). Dynamics of an expanding circular fault. Bulletin of the Seismological Society of America, 66(3), 639-666.

Majstorović, J., Giffard-Roisin, S., & Poli, P. (2021). Designing Convolutional Neural Network Pipeline for Near-Fault Earthquake Catalog Extension Using Single-Station Waveforms. Journal of Geophysical Research: Solid Earth, 126(7), e2020JB021566.

Marsan, D., & Nalbant, S. S. (2005). Methods for measuring seismicity rate changes: a review and a study of how the M w 7.3 landers earthquake affected the aftershock sequence of the M w 6.1 Joshua Tree earthquake. Pure and Applied Geophysics, 162(6), 1151-1185.

Mirabella, F., Ciaccio, M. G., Barchi, M. R., & Merlini, S. (2004). The Gubbio normal fault (Central Italy): geometry, displacement distribution and tectonic evolution. Journal of Structural Geology, 26(12), 2233-2249.

Nadeau, R. M., & McEvilly, T. V. (1999). Fault slip rates at depth from recurrence intervals of repeating microearthquakes. Science, 285(5428), 718-721.

Obara, K. (2002). Nonvolcanic deep tremor associated with subduction in southwest Japan. Science, 296(5573), 1679-1681.

Omori, F. (1894). On after-shocks. Seismological journal of Japan, (19), 71-80.

Pauselli, C., Barchi, M. R., Federico, C., Magnani, M. B., & Minelli, G. (2006). The crustal structure of the Northern Apennines (Central Italy): an insight by the CROP03 seismic line. American Journal of Science, 306(6), 428-450.

Peng, Z., & Zhao, P. (2009). Migration of early aftershocks following the 2004 Parkfield earthquake. Nature Geoscience, 2(12), 877-881.

Perfettini, H., & Avouac, J. P. (2004). Postseismic relaxation driven by brittle creep: A possible mechanism to reconcile geodetic measurements and the decay rate of aftershocks, application to the Chi-Chi earthquake, Taiwan. Journal of Geophysical Research: Solid Earth, 109(B2).

Piana Agostinetti, N., Giacomuzzi, G., & Chiarabba, C. (2017). Seismic swarms and diffuse fracturing within Triassic evaporites fed by deep degassing along the low-angle Alto Tiberina normal fault (central Apennines, Italy). Journal of Geophysical Research: Solid Earth, 122(1), 308-331.

Pinzon-Rincon, L., Lavoué, F., Mordret, A., Boué, P., Brenguier, F., Dales, P., ... & Hollis, D. (2021). Humming trains in seismology: an opportune source for probing the shallow crust. Seismological Research Letters, 92(2A), 623-635.

Poli, P., Boaga, J., Molinari, I., Cascone, V., & Boschi, L. (2020). The 2020 coronavirus lockdown and seismic monitoring of anthropic activities in Northern Italy. Scientific Reports, 10(1), 1-8.

Poli, P., Cabrera, L., Flores, M. C., Báez, J. C., Ammirati, J. B., Vásquez, J., & Ruiz, S. (2022). Volcanic origin of a long-lived swarm in the Central Bransfield Basin, Antarctica. Geophysical Research Letters, e2021GL095447.

Rietbrock, A., Tiberi, C., Scherbaum, F., & Lyon-Caen, H. (1996). Seismic slip on a low angle normal fault in the Gulf of Corinth: Evidence from high-resolution cluster analysis of microearthquakes. Geophysical Research Letters, 23(14), 1817-1820.

Ruhl, C. J., Abercrombie, R. E., Smith, K. D., & Zaliapin, I. (2016). Complex spatiotemporal evolution of the 2008 Mw 4.9 Mogul earthquake swarm (Reno, Nevada): Interplay of fluid and faulting. Journal of Geophysical Research: Solid Earth, 121(11), 8196-8216.

Sánchez-Reyes, H., Essing, D., Beaucé, E., & Poli, P. (2021). The imbricated foreshock and aftershock activities of the Balsorano (Italy) Mw 4.4 normal fault earthquake and implications for earthquake initiation. Seismological Research Letters, 92(3), 1926-1936.

Schoenball, M., & Ellsworth, W. L. (2017). A systematic assessment of the spatiotemporal evolution of fault activation through induced seismicity in Ok-

lahoma and southern Kansas. Journal of Geophysical Research: Solid Earth, 122(12), 10-189.

Scholz, C. H. (2019). The mechanics of earthquakes and faulting. Cambridge university press.

Seno, T., & Yamasaki, T. (2003). Low-frequency tremors, intraslab and interplate earthquakes in Southwest Japan—from a viewpoint of slab dehydration. Geophysical Research Letters, 30(22).

Serpelloni, E., Anzidei, M., Baldi, P., Casula, G., & Galvani, A. (2005). Crustal velocity and strain-rate fields in Italy and surrounding regions: new results from the analysis of permanent and non-permanent GPS networks. Geophysical Journal International, 161(3), 861-880.

Shelly, D. R. (2020). A high-resolution seismic catalog for the initial 2019 Ridgecrest earthquake sequence: Foreshocks, aftershocks, and faulting complexity. Seismological Research Letters, 91(4), 1971-1978.

Shelly, D. R., Beroza, G. C., Ide, S., & Nakamula, S. (2006). Low-frequency earthquakes in Shikoku, Japan, and their relationship to episodic tremor and slip. Nature, 442(7099), 188-191.

Shelly, D. R., & Johnson, K. M. (2011). Tremor reveals stress shadowing, deep postseismic creep, and depth-dependent slip recurrence on the lower-crustal San Andreas fault near Parkfield. Geophysical Research Letters, 38(13).

Tan, Y. J., & Marsan, D. (2020). Connecting a broad spectrum of transient slip on the San Andreas fault. Science advances, 6(33), eabb2489.

Thomas, A. M., Beeler, N. M., Bletery, Q., Burgmann, R., & Shelly, D. R. (2018). Using low-frequency earthquake families on the San Andreas Fault as deep creepmeters. Journal of Geophysical Research: Solid Earth, 123(1), 457-475.

Trugman, D. T., Wu, C., Guyer, R. A., & Johnson, P. A. (2015). Synchronous low frequency earthquakes and implications for deep San Andreas Fault slip. *Earth and Planetary Science Letters*, *424*, 132-139.

Uchida, N., & Bürgmann, R. (2019). Repeating earthquakes. Annual Review of Earth and Planetary Sciences, 47, 305-332.

Uieda, L., Tian, D., Leong, W. J., Toney, L., Schlitzer, W., Grund, M., ... & Wessel, P. (2021). PyGMT: A Python interface for the generic mapping tools.

Vadacca, L., Casarotti, E., Chiaraluce, L., & Cocco, M. (2016). On the mechanical behaviour of a low-angle normal fault: the Alto Tiberina fault (Northern Apennines, Italy) system case study. Solid Earth, 7(6), 1537-1549.

Valoroso, L., Chiaraluce, L., Di Stefano, R., & Monachesi, G. (2017). Mixed-mode slip behavior of the Altotiberina low-angle normal fault system (Northern Apennines, Italy) through high-resolution earthquake locations and

repeating events. Journal of Geophysical Research: Solid Earth, 122(12), 10-220.

Vuan, A., Brondi, P., Sugan, M., Chiaraluce, L., Di Stefano, R., & Michele, M. (2020). Intermittent Slip Along the Alto Tiberina Low-Angle Normal Fault in Central Italy. Geophysical Research Letters, 47(17), e2020GL089039.

Wernicke, B. (1995). Low-angle normal faults and seismicity: A review. Journal of Geophysical Research: Solid Earth, 100(B10), 20159-20174.

Wu, C., Guyer, R., Shelly, D., Trugman, D., Frank, W., Gomberg, J., & Johnson, P. (2015). Spatial-temporal variation of low-frequency earthquake bursts near Parkfield, California. Geophysical Journal International, 202(2), 914-919.

Dynamics of the Seismicity in the Alto Tiberina Fault System revealed by a High-Resolution Template Matching Catalog

David Essing[1*], Piero Poli[1]

[1]ISTerre Institut des Sciences de la Terre, CNRS, Université Grenoble Alpes, France.

Corresponding author: David Essing (david.essing@univ-grenoble-alpes.fr)

Université Grenoble Alpes, ISTerre CS 40700 38058, GRENOBLE Cedex 9

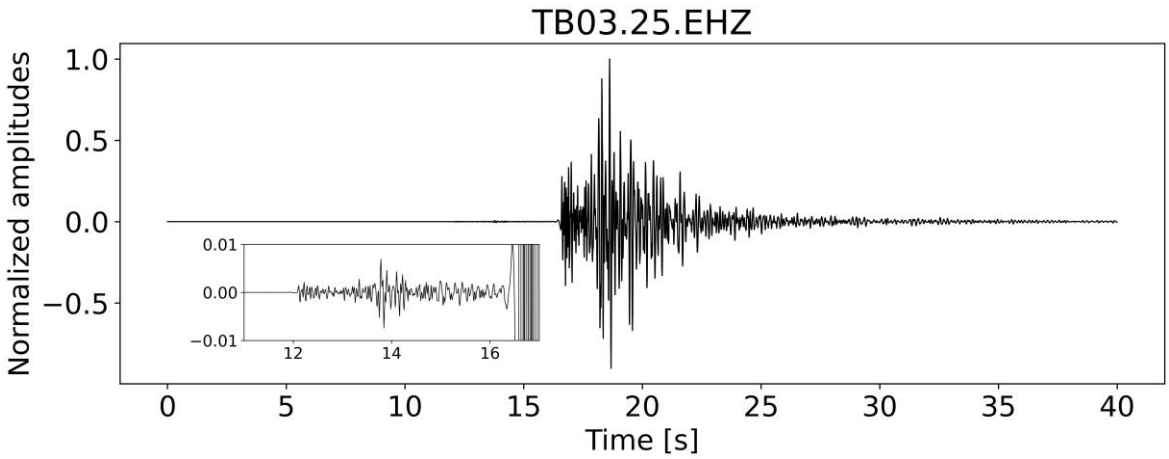

Figure S1: Normalized waveform of a M= 2.8 event (2014-12-20T12:14:24) at station TB03.25. The zoomed inset allows to see a smaller event M∼−0.2 preceding the larger event by 3s. Notably, both events share elevated similarity in terms of waveforms having a high CC of ∼0.66.

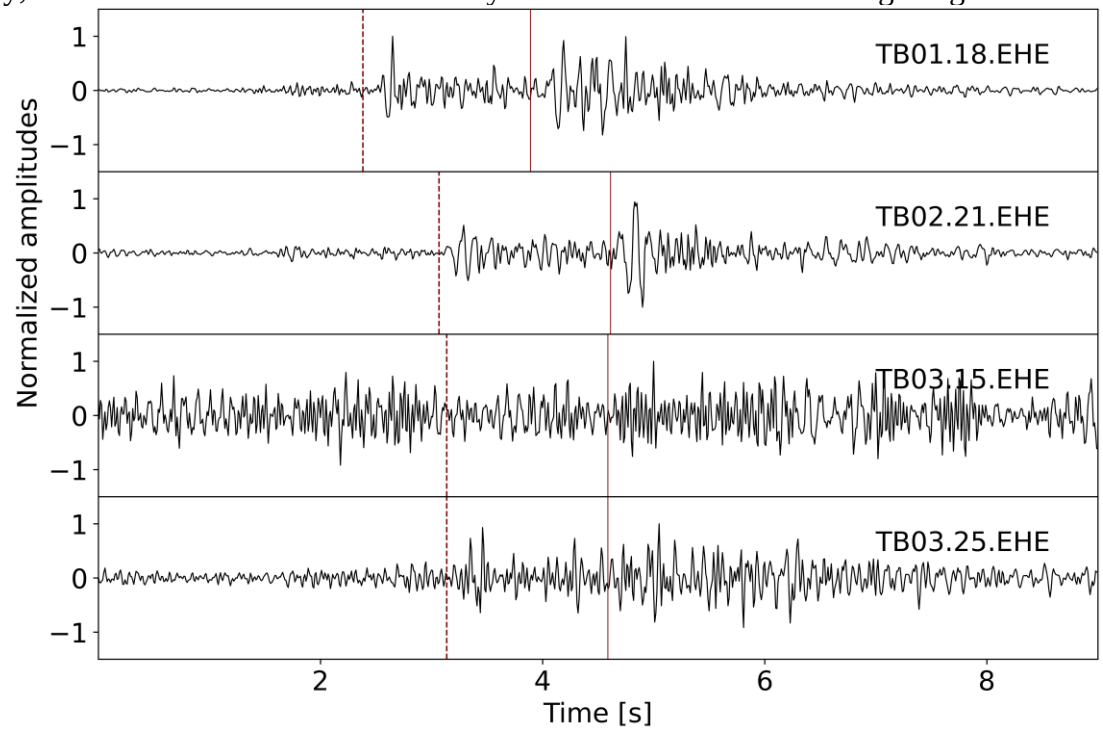

Figure S2: Normalized waveforms for the East components of all used stations of two consecutive events (2013-12-21T22-57-54.75 and 2013-12-21T22-57-56.33) following each other by ~ 1.5s. The red dashed line indicates the theoretical s-wave arrival time assuming the travel time of the detecting template. The red solid line indicates the same but for the second template.

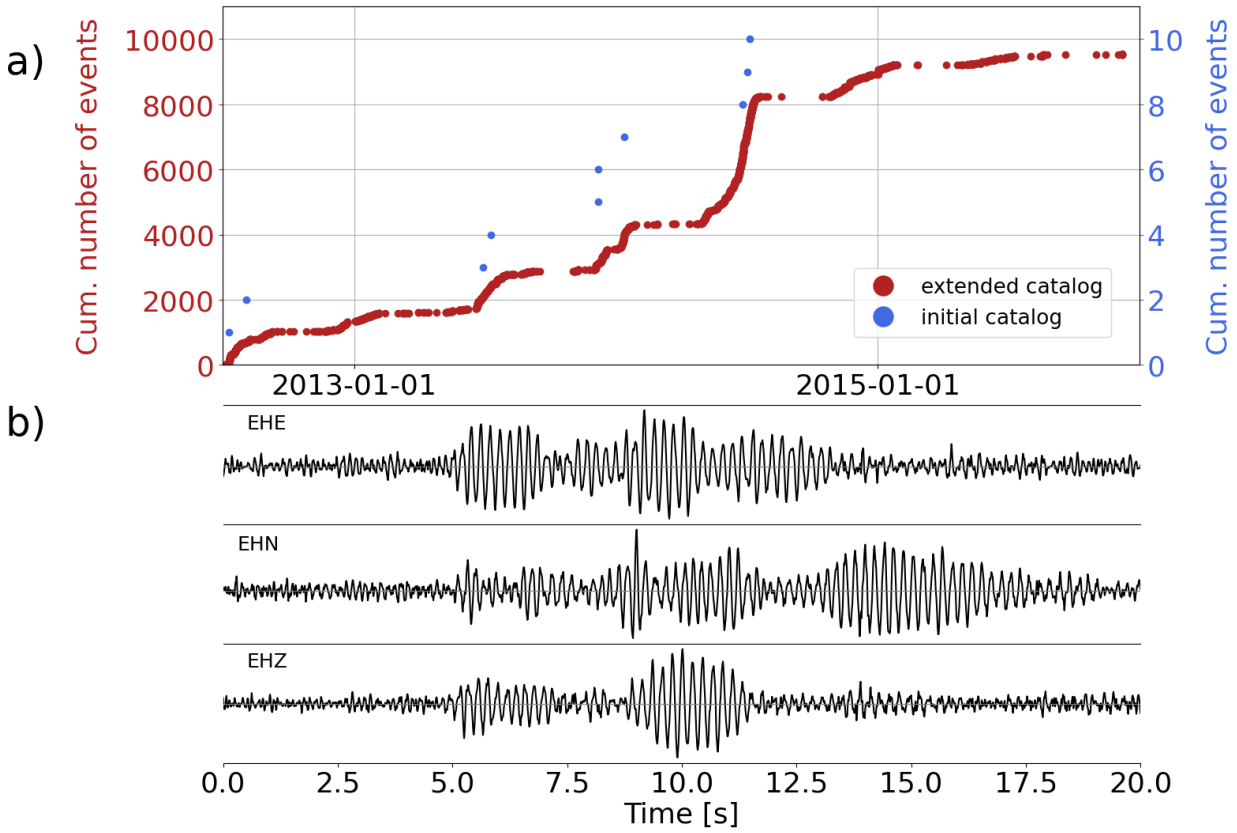

Figure S3: (a) Cumulative number of events as a function of time for events radiated at shallow depths close to a cement factory in the southern part of the Gubbio basin. Note the different scale for the two catalogs. (b) Normalized three-component waveforms recorded at TB02 for one of the events.

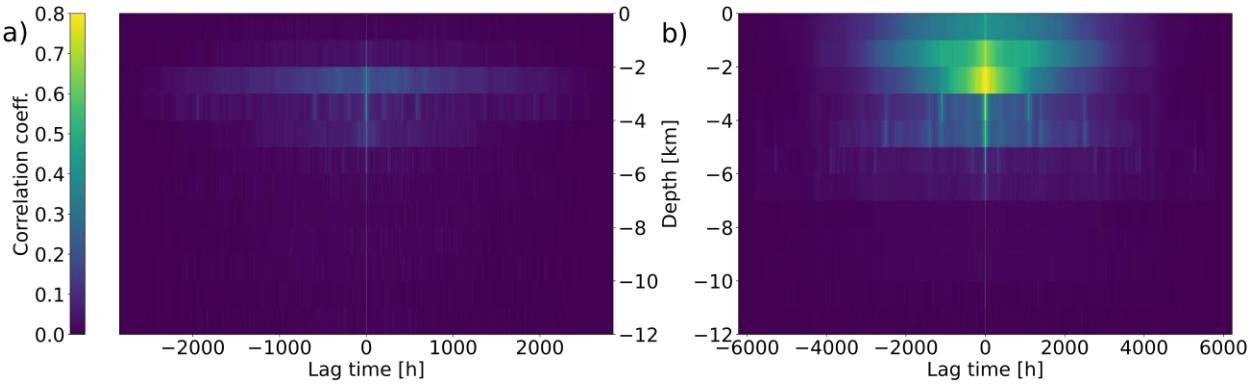

Figure S4: Auto-correlation functions of the event count time series binned in 1 km along depth and 1-hour lasting time bins for (a) the pre-swarm and (b) the swarm time period. For both plots, the color-bar ranges from 0 to 0.8.

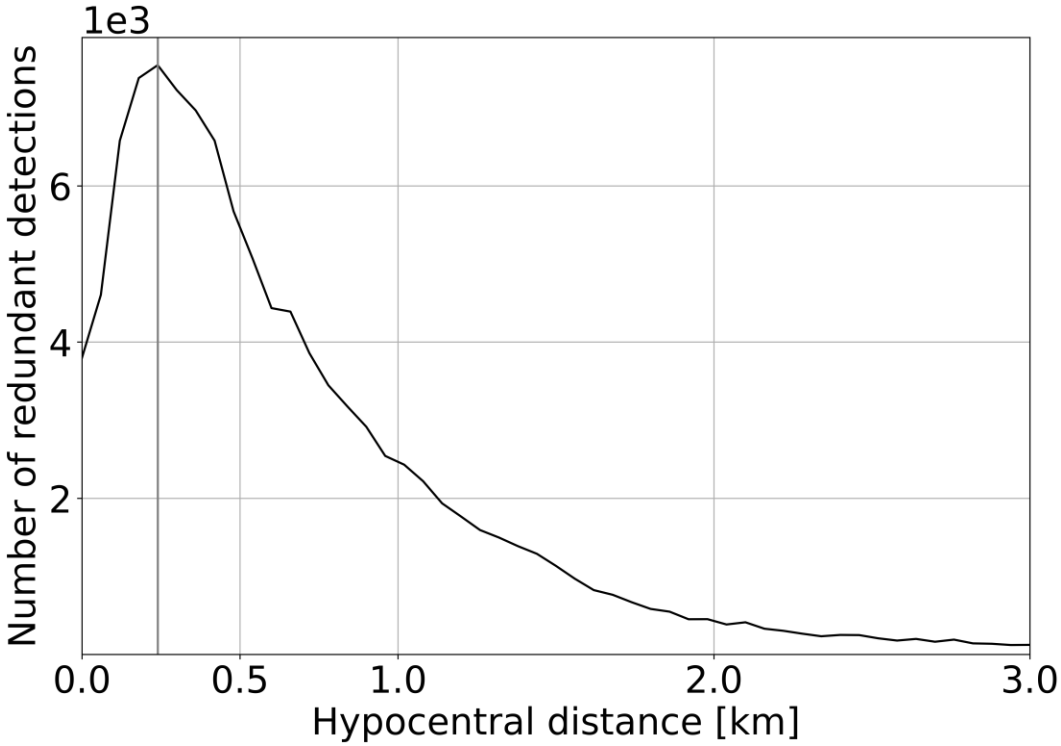

Figure S5: Number of redundant detections as a function of hypo-central distance between the redundant detection and the auto-detection

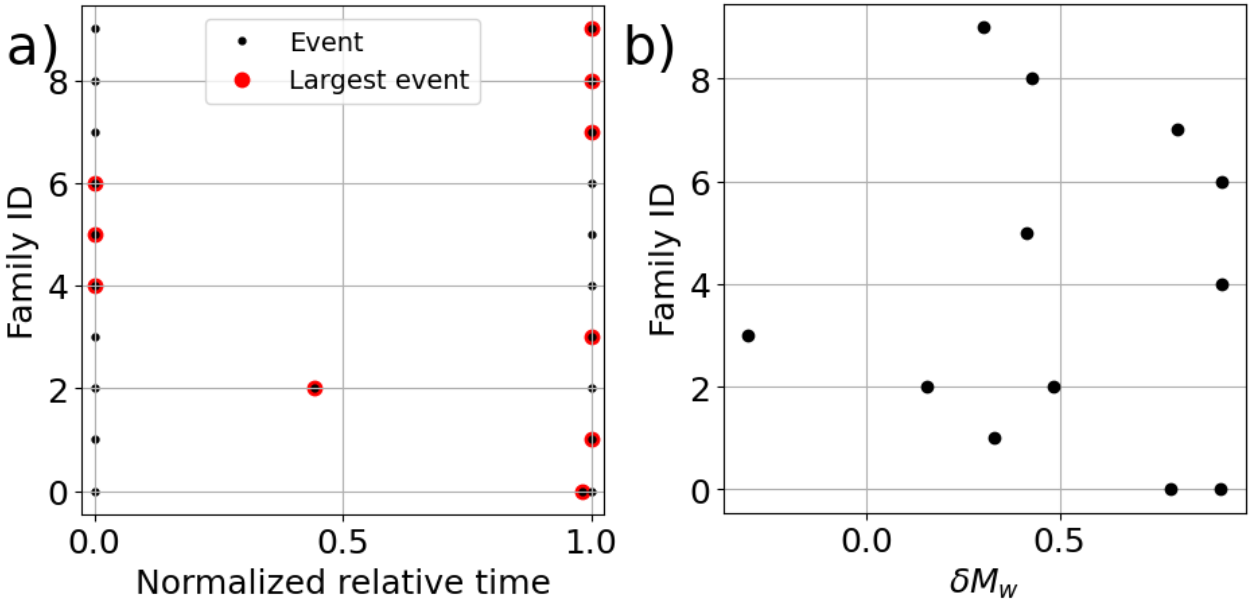

Figure S6: (a) Normalized relative times for each family of repeating events. Red dots indicate the largest event within a family. (b) The difference between the largest event and the other events within each family in δM_w

Table S1: 1-d p wave velocity model (Chiaraluce et. al, 2007)

Layer top [km]	p-wave velocity [km/s]
0	4.6
3	5.5
5	6.0
7	6.7
38	7.9

Table S2: Families of repeating events. If events within a family were detected by different templates, they have different locations. In this case we computed the average location between them.

lat [deg]	lon [deg]	depth [km]	origin time first event	duration [s]	nr_events
43.4360707601	12.598309199	8.76996	2013-03-15T07:36:33	9965.625624	3
43.4151954651	12.5473885536	8.21381	2013-03-16T09:17:48	16.418728	2
43.2324930827	12.7999251684	9.35883	2013-03-16T23:07:36	1110.068787	3
43.2407913208	12.6791934967	8.37477	2013-05-17T22:17:12	4722.86	2
43.3787097931	12.7431268692	12.170995	2013-09-14T19:19:33	240.38526	2
43.4539909363	12.5763912201	8.512165	2013-09-21T17:08:56	4942.709734	2
43.3979263306	12.6931066513	9.59176	2014-11-22T03:42:20	100.95	2
43.2024154663	12.6606607437	8.59461	2015-02-18T10:14:04	1798.788118	2
43.4421749115	12.6010336876	9.163845	2015-07-31T19:30:15	1366.510071	2
43.436630249	12.6200275421	9.175625	2015-08-09T23:21:46	1836.393349	2

Logistic function used to weight the maxima of each component wise cross-correlation function depending on the SNR of the correlated waveforms (for more details see Duverger et al., 2018)

$$f(x) = \frac{L}{1+e^{-k(x-x_0)}} \quad (1)$$

Where $L = 1$, $k = 2.5$, and $x_0 = 3$ (Duverger et al., 2020).

Reference

Chiaraluce, L., Chiarabba, C., Collettini, C., Piccinini, D., & Cocco, M. (2007). Architecture and mechanics of an active low-angle normal fault: Alto Tiberina fault, northern Apennines, Italy. Journal of Geophysical Research: Solid Earth, 112(B10).

Duverger, C., Lambotte, S., Bernard, P., Lyon-Caen, H., Deschamps, A., & Nercessian, A. (2018). Dynamics of microseismicity and its relationship with the active structures in the western Corinth Rift (Greece). Geophysical Journal International, 215(1), 196-221.